# Displacement patterns of a Newtonian fluid by a shearthinning fluid in a rough fracture

Le Zhang, Zhibing Yang, Yves Méheust, Insa Neuweiler, Ran Hu, Yi-Feng Chen

# Displacement patterns of a Newtonian fluid by a shear-thinning fluid in a rough fracture

Le Zhang[1, 2], Zhibing Yang[1, 2, *], Yves Méheust[3], Insa Neuweiler[4], Ran Hu[1, 2], Yi-Feng Chen[1, 2]

1 State Key Laboratory of Water Resources Engineering and Management, Wuhan University, Wuhan 430072, China

2 Key Laboratory of Rock Mechanics in Hydraulic Structural Engineering of the Ministry of Education, Wuhan University, Wuhan 430072, China

3 University of Rennes, CNRS, Géosciences Rennes (UMR 6118), Rennes, France

4 Institute of Fluid Mechanics Environmental Physics in Civil Engineering, Leibniz University Hannover, Hannover, Germany

* Corresponding author: zbyang@whu.edu.cn (Z. Yang)

Key points

- We conduct drainage experiments in which a shear-thinning fluid displaces a Newtonian fluid in a transparent rough fracture
- We present an experimental phase diagram of displacement patterns in the space of flow rate and shear-thinning rheological property
- We propose a theoretical model of stability criterion and elucidate the mechanisms behind the flow regime transitions

This article has been accepted for publication and undergone full peer review but has not been through the copyediting, typesetting, pagination and proofreading process, which may lead to differences between this version and the Version of Record. Please cite this article as doi: 10.1029/2023WR034958.

**Abstract**

Two-phase flow involving non-Newtonian fluids in fractured media is of vital importance in many natural processes and subsurface engineering applications, such as rock grouting, groundwater remediation, and enhanced oil recovery. Yet, how the displacement dynamics is impacted by the non-Newtonian rheology remains an open question. Here, we conduct primary drainage experiments in which a shear-thinning Xanthan gum solution displaces a silicone oil in a transparent rough fracture for a wide range of shear-thinning property (controlled by polymer concentration) and flow rates. We first evaluate the effects of shear-thinning property on displacement efficiency. Based on qualitative and quantitative analyses of the observed fluid morphologies, we present an experimental phase diagram of the obtained displacement patterns. We characterize a novel displacement pattern where the fluid-fluid interface changes from stable (plug flow) to unstable (fingering) as the fracture aperture, averaged over the transverse direction, varies along the mean flow direction. We demonstrate that the existence of this mixed displacement pattern can be explained by local viscosity heterogeneity induced by the coupling of the shear-thinning behavior and the spatial variability of apertures. Finally, we propose a theoretical model elucidating the mechanisms behind the flow regime transitions. The interface stability criterion predicted by this model exhibits good agreement with the experimental measurements, and stresses the potentially important role of fluid rheology, coupled to aperture variability, in immiscible displacements in rough fractures. These findings provide new insights into the dynamics of immiscible two-phase flows with non-Newtonian effects, and has potential implications for the aforementioned engineering applications.

# 1. Introduction

The flow of complex fluids in rock fractures is of significant importance in many industrial and environmental applications, such as enhanced oil recovery (EOR) (Sorbie, 2013), hydraulic fracturing (Raimbay et al., 2016), rock grouting (Zou et al., 2018), and soil remediation (Tosco and Sethi, 2010). Many of the complex fluids involved in these applications exhibit a shear-thinning behavior (i.e., their viscosity decreases as the imposed shear rate increases), e.g., polymer solutions, heavy oils, slurries, foams, gels (Lindner et al., 2000; Lavrov, 2013; Coussot, 2014; Poole, 2016; De et al., 2017). Shear-thinning fluids are commonly employed for oil recovery and soil remediation to improve the sweep efficiency of the reservoir due to their ability to stabilize the displacement front (Auradou et al., 2008; Silva et al., 2012). In hydraulic fracturing, the shear-thinning property of the carrier fluid contributes to decreasing the viscosity, resulting in lower hydraulic resistance, which can enhance proppant transport and provide a high-permeability conductive path for reservoir fluids (Barbati et al., 2016; Lavrov, 2013; Osiptsov, 2017). Therefore, understanding the flow dynamics of complex shear-thinning fluids during immiscible fluid-fluid displacement in rough fractures is of vital importance for controlling interfacial patterns of two-phase flow involving non-Newtonian fluids and, more generally, for predicting and understanding the dynamics of multiphase flow in subsurface engineering applications.

Immiscible two-phase flow in single fractures has gained a broad attention over the last decades, and extensive studies have provided a basic understanding of fluid invasion behaviors in rough fractures (Persoff and Pruess, 1995; Glass et al., 1998; Amundsen et al., 1999;

Berkowitz, 2002; Yang et al.,2013; Chen et al., 2017; Hu et al., 2018; Silva et al., 2019). In the absence of gravity (e.g., for horizontal fractures or fluids of similar density), various immiscible displacement patterns, ranging from capillary to viscous fingering to compact displacement, are mainly controlled by the interplay between capillary and viscous forces (Detwiler et al., 2009; Hu et al., 2019; Yang et al., 2019b), which, similarly to what has been well known for two-dimensional porous media (Lenormand et al., 1988), can be quantified by two dimensionless numbers: the capillary number *Ca* and the viscosity ratio *M* between the two phases. Chen et al. (2017, 2018) conducted a series of experiments from favorable to unfavorable conditions to study the transition between these flow patterns through flow-visualization experiments in a transparent fracture and presented a full phase diagram mapping these three patterns in the *M–Ca* plane, for a rough fracture geometry obtained by molding a real rock fracture. The spatial variability of the aperture field is another important factor that influences two-phase flow in rough fractures, impacting the displacement patterns and phase distribution together with the *Ca* and *M* (Yang et al., 2016; 2019a; Hu et al., 2019). However, most of the studies of multiphase flow in fractured media have focused on Newtonian fluids, whose viscosity is independent of shear rate. The monophasic flow of shear-thinning fluids in rough fractures has been studied using lubrication (i.e., depth-averaged) models for power law fluids (Lavrov, 2013) as well as more realistic rheology characteristic of xanthan gum (Lenci et al., 2022a) but the displacement characteristics of multiphase flow involving shear-thinning fluids in rough fractures remain poorly understood.

When non-Newtonian fluids are involved in the multiphase flow process, coupling

between the complex rheological behavior and the fracture's aperture heterogeneity may produce unexpected flow regimes. Numerous experimental and theoretical studies on shear-thinning fluids flow in Hele-Shaw cells or porous media have been conducted in order to explain the correlation between flow patterns and fluid rheology (Nittmann et.al., 1985; Buka et al., 1986; Lemaire et al., 1991; Shah and Yortsos, 1995; Kondic et al., 1998; Coussot, 1999; Mehr et al., 2020; Rodríguez de Castro and Goyeau, 2022). Significant differences of morphological patterns in Hele-Shaw cells induced by the non-Newtonian rheology of the displacing or displaced fluids have been observed, e.g., snowflake-like patterns (Buka et al.,1986), fractal patterns (Nittmann et al., 1985) and fracture-like patterns (Lemaire et al., 1991). In particular, shear-thinning properties have been shown to suppress tip-splitting (Fast et al.,2001), produce oscillating fingers and side branches during growth (Kondic et al., 1998), and narrow or widen the width of fingers (Bonn et al., 1995; Kawaguchi et al., 1997).

In contrast to what occurs in Hele-Shaw cells, in porous media the viscosity of non-Newtonian fluids depends on the mean interstitial velocity (which controls the local shear rate). Due to the complexity and diversity of the void space geometry of porous media, injection of non-Newtonian fluids can result in a wide range of local viscosities and strong viscosity heterogeneity, with a general monophasic flow behavior of stronger flow localization as compared to Newtonian flow in the same medium (Shah and Yortsos, 1995; Zami-Pierre et al., 2016; Hauswirth et al., 2019; Airiau and Bottaro, 2020). For two-phase flow configurations, more marked preferential flow paths (the connected regions of high velocity) and more complex fingering patterns are observed when non-Newtonian fluids flow in porous media

(Géraud et al., 2016; An et al., 2022).

In rough fractures, the coupling of shear-thinning rheology and heterogeneity of fractures induces a more pronounced channelization phenomenon as compared to Newtonian flow in the same geometry (Zhang et al., 2019). However, for rough fractures with various aperture heterogeneity, the transmissivity attenuation due to flow channelization is compensated by the fluid shear-thinning rheology (Lenci et al., 2022a), which can render the transmissivity up to several orders of magnitude larger than its Newtonian counterpart (note that the transmissivity is not intrinsic, it depends on the imposed macroscopic pressure gradient (Lenci et al., 2022b). Rodríguez de Castro and Radilla (2017) conducted shear-thinning fluid flow experiments through rough fractures and proposed a method to predict the macroscopic pressure drop. Much of the research on shear-thinning fluid flow behavior and local flow fields in rough fractures is mainly through numerical simulations (Yan and Koplik, 2008; Lavrov, 2013; Boronin et al., 2015; Zhang et al., 2019). Experimental work by Boschan et al. (2007) investigated the influence of fluid rheology on the propagation of a displacement front during miscible displacements in a rough-walled fracture. To our knowledge, for immiscible displacement, visualization and quantification of the displacement patterns involving non-Newtonian fluids in rough fractures have been rarely reported. A fundamental understanding of the rheological effects in multiphase flow through fractured media is still lacking.

In this work, we perform well controlled flow-visualization experiments of a Xanthan gum solution displacing silicone oil in a transparent fracture replica, with the aim of elucidating the mechanisms of immiscible displacement involving a shear-thinning rheology of the

displacing fluid. We obtain an experimental phase diagram of displacement patterns and quantify the corresponding displacement efficiency of shear-thinning fluids as functions of *Ca* and *M*. In particular, a new displacement pattern is observed and qualified by analyzing the evolutions of the normalized front tip with the specific interface length. A theoretical criterion based on the linear stability analysis is proposed to evaluate the interface stability, and the factors influencing the flow regime transitions are analyzed.

# 2. Materials and Methods

## 2.1 Experiment Setup

The schematic of the flow visualization apparatus is shown in the Supplementary Information (SI) Figure S1, which includes a rough fracture flow cell, imaging equipment, and a fluid injection system. The transparent fracture cell is mounted on a platform. A CMOS camera (ORCA-Flash4.0, HAMAMATSU) and a LED panel are installed above and below the fracture, respectively. The camera is used to acquire images during the displacement, with a spatial resolution of 72.2 μm per pixel. The syringe pump A (Harvard apparatus 70-3007) is used to saturate the fracture with silicone oil to maintain an initially oil-saturated state. The syringe pump B (Harvard apparatus 70-3007) is used to inject a dyed Xanthan gum solution (shear thinning) to displace the silicone oil. In addition, a pressure sensor (uPS0250-T116, LabSmith) with a resolution of 1 Pa is installed at the inlet to measure the pressure drop over the fracture.

A series of drainage experiments are conducted in the rough fracture consisting of two rough

epoxy resin replicas fabricated from a rock fracture in a granite sample. The fracture is 14 cm long and 6.6 cm wide. The fabrication procedure of the two fracture replicas is similar to the method reported in Isakov et al. (2001); the detailed process is shown in SI Figure S2. The aperture field is measured by using an image processing procedure based on the attenuation law of Beer-Lambert. The aperture field and the aperture histogram of the fracture are presented in Figure 1a, c. The aperture field exhibits spatial variability, with a mean aperture $<b> = 0.283$ mm, a standard deviation $\sigma_b = 0.039$ mm, and a relatively low fracture closure parameter (de Dreuzy et al., 2012) defined as the ratio of the standard deviation to the mean aperture ($\sigma_b/<b>$ less than 0.2). The fracture has no contact points but its aperture variability is still significant since the difference between its maximum and its minimum apertures is much larger than the standard deviation of the aperture field. The fracture's void space has a volume of $V_f = 2.6$ ml. Figure 1b presents the average aperture profile $b_x$ along the mean flow direction; its shows that the apertures are on average smaller at the center of the fracture, whereas larger apertures on average are found near the inlet and outlet of the fracture. Based on this feature of the aperture field, we divide the fracture plane into three regions (A1, A2, A3), among which A1 and A3 display a strong trend of the longitudinal profile of the transversally-averaged apertures ($\alpha_{A1} = -1.43\times10^{-3}$ and $\alpha_{A3} = 1.45\times10^{-3}$, respectively), and A2 is an area with relatively uniform aperture along the flow direction. Here the mean aperture gradient/trend is defined as $\alpha = \Delta h/\Delta L$, where $\Delta h$ is the variation of mean aperture (averaged over the transverse direction) along a distance $\Delta L$ (larger than the scale of local aperture variations, i.e., a few millimeters in this study) in the flow direction. A positive value of $\alpha$ indicates an increase in transversally-

averaged aperture profile as a function of the longitudinal coordinate (left to right on the Fig. 1B) while a negative value indicates a decrease. The spatial correlations within the aperture fields have been analyzed from the Fourier density spectrum. It shows that no correlation length is visible, indicating that the two fracture walls are entirely uncorrelated with each other; in addition, they both exhibit a self-affine scale invariance with a Hurst exponent slightly above 0.5. The Hurst exponent of natural rock fractures typically ranges from 0.45 to 0.8 (Odling, 1994; Schmittbuhl et al., 2008) and this value is within the range, though for granite it is usually closer to 0.8 (Schmittbuhl et al., 2008)

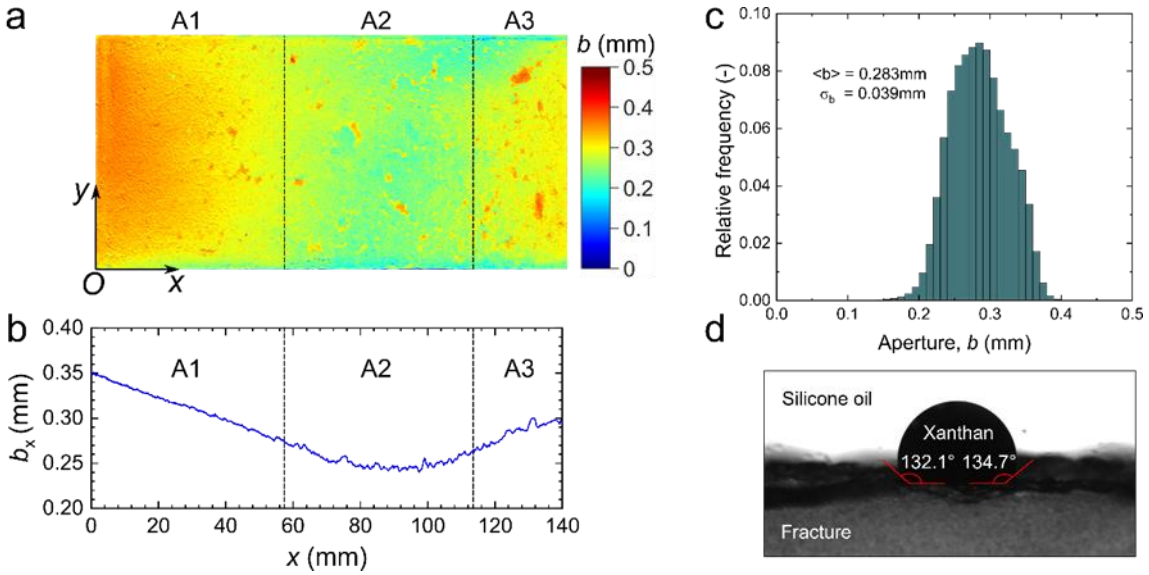


**Figure 1.** (a) Aperture field measured by light transmission technique. The three divided regions (A1, A2, A3) are based on the characteristics of the aperture field. (b) Average aperture profile along the flow direction. (c) Histogram of apertures. (d) Measurement of the contact angle based on the images of a small Xanthan solution drop placed on the rough fracture surface submerged in an oil-filled reservoir.

## 2.2 Fluid properties

In our experiments, the defending fluid is (Newtonian) silicone oil with a dynamic viscosity of 1000 mPa·s, and the invading fluids are aqueous solutions with dissolved Xanthan gum powder concentrations of 0.3, 0.5, and 1 wt%. Using the Drop Shape Analyzer (KRÜSS, DSA25E), the measured three-phase contact angle between the polymer solution and the rough fracture surface in the presence of silicone oil is $\theta = 133\pm2°$ (Figure 1d) and the interfacial tension is 26±1 mN/m. The polymer solutions are dyed with a tracer (Carmine, Wilton) at a concentration 0.2 wt%, to offer a good contrast for visualization. The most important rheological properties of Xanthan gum include high viscosity at low concentrations, pronounced shear-thinning behavior, and good resistance to shear degradation (Whitcomb and Macosko,1978). Due to its exceptional rheological properties and non-toxicity to living organisms, Xanthan gum is widely used as an effective stabilizer or a suitable thickener for various kinds of water-based systems (Song et al., 2006; Silva et al., 2012). The Herschel-Bulkley model (Herschel and Bulkley, 1926) has been considered as an applicable model to describe the rheological behavior of concentrated Xanthan gum solutions (Song et al., 2006; Rodríguez de Castro and Radilla, 2017). It has the advantage of simplicity, though models such as the Ellis and Carreau models, which describe the transition from a constant viscosity plateau at low shear rates to a power law dependence of the viscosity on shear rate at larger shear rate, provide the best match to rheological data (Lenci et al., 2022a).

The polymer solutions are prepared by dissolving Xanthan gum powder in deionized water with an electronic blender. Once fully dissolved, the polymer solution is put into a

vacuum drying oven to eliminate air bubbles. Finally, the degassed solution is put to rest for 24 hours before taking the rheological measurements of the resulting Xanthan gum solutions. These measurements are obtained by using a hybrid rheometer (DHR-2, TA Instrument) equipped with a cone-plate geometry at a constant temperature of 25±1°C.

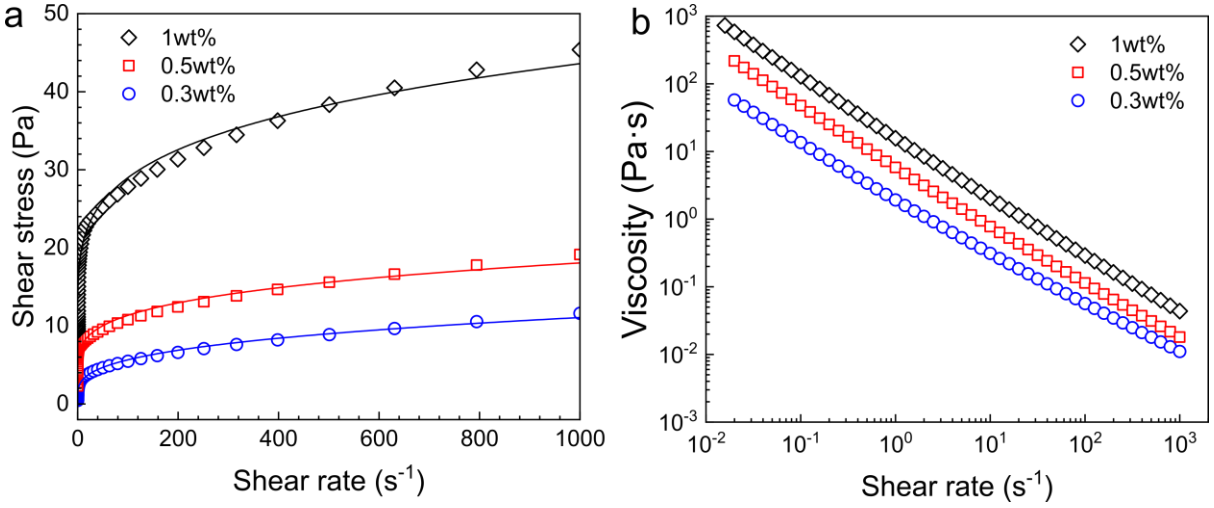


**Figure 2.** (a) Flow curves of shear stress versus shear rate. The solid lines correspond to the fitted Herschel–Bulkley model data (Eq. (1)). (b) The calculated viscosity as a function of the shear rate based on the model.

Figure 2a displays the rheometer flow curves of the Xanthan gum solutions with different concentrations. As shown in Figure 2a, at low shear rates, each of these fluids exhibits a yield stress which is enhanced by increasing the polymer concentration. The data can be well fitted by using the Herschel–Bulkley model:

$$\tau = \tau_c + k\dot{\gamma}^n \qquad (1)$$

where $\tau_c$ is the yield stress, $k$ is the fluid consistency index, and $n$ is the power-law index. The values of $\tau_c$, $k$, and $n$ are controlled by the polymer concentration under given pressure and temperature conditions. The Herschel–Bulkley viscosity $\mu(\dot{\gamma})$, which depends on the polymer

concentration and the shear rate $\dot{\gamma}$ , is calculated as:

$$\mu(\dot{\gamma}) = \tau_c \dot{\gamma}^{-1} + k\dot{\gamma}^{n-1} \quad (2)$$

The dependence of the Herschel–Bulkley viscosity on shear rate is shown in Figure 2b according to Eq. (2). Figure 2b illustrates that higher concentrations result in higher viscosities and that the viscosity of the solutions strongly decreases with the shear rate. For $C_p$ = 0.3wt%, $\tau_c$ = 0.857 Pa, $n$ = 0.3279, $k$ = 1.061 Pa·s$^n$; for $C_p$ = 0.5wt%, $\tau_c$ = 3.548 Pa, $n$ = 0.2695, $k$ = 2.257 Pa·s$^n$; for $C_p$ = 1.0wt%, $\tau_c$ = 9.040 Pa, $n$ = 0.2385, $k$ = 6.652 Pa·s$^n$.

To guarantee the consistency of fluid properties under the same concentration and various flow rate conditions, we let the polymer solutions stand for 24 hours after preparation using the above setups before conducting experiments, and the experiments for the solutions with the same concentration are performed in one day. In the meantime, same experimental protocols were used to ensure uniformity of the initial conditions of experiments. To check the mechanical degradability of the polymer solutions, the effluent fluid collected at the outlet of the fracture after single-phase flow of xanthan gum solutions has been analyzed. No significant change was observed between the rheograms of the invading fluid and the effluent fluid, demonstrating that mechanical degradation during the experiments was negligible. Moreover, the experiment of displacing silicone oil (20 mPa·s) with water-glycerol mixtures (400 mPa·s) is supplemented as a contrasting experiment, i.e., for comparison.

## 2.3 Experimental procedure

In our experiments, silicone oil is the defending fluid (and the wetting phase, hence the

displacement is a drainage process) and three polymer solutions with respective mass fractions of Xanthan gum powder 0.3wt%, 0.5wt% and 1wt% are used as invading fluid (and non-wetting phase). The concentrations of these polymer solutions have been selected to attain a viscosity range, when changing the imposed shear rate, which contains the viscosity of the silicone oil. In this way, the viscosity ratio above or below unity depends on the flow rate (or shear rate). Thus, it is possible to observe the transition from stable interface displacement to viscous fingering under these combinations of fluid pairs.

For each experiment, the fracture cell is initially fully saturated with silicone oil at a flow rate of 5 mL/min by using the syringe pump A. Then, the syringe pump B is used to inject the dyed Xanthan solution at a constant flow rate (0.1, 0.5, 1, 5, 10 mL/min, corresponding to a Darcy velocity between 0.072 mm/s and 7.2 mm/s) and allow it to displace the resident silicone oil until breakthrough occurs (i.e., the invading fluid reaches the outlet of the fracture cell). During the displacement process, images of invasion morphologies are recorded at 10 frames/s with the CMOS camera and the longitudinal pressure drops $\Delta P$ over the fracture cell are measured every half second by the pressure sensor. A cleaning procedure is followed after each experiment. This procedure consists of three steps: (1) injecting deionized water into the fracture at a high flow rate of 20 mL/min for 20 minutes to dilute the Xanthan solution; (2) drying the fracture cell using a vacuum drying oven; and (3) injecting silicone oil at a flow rate of 5 mL/min for 10 minutes to displace the resident water and saturate the fracture cell. The room temperature during the experiments was maintained at 25±1 °C. The above experimental protocol was repeated for the three selected Xanthan solutions, and hence a total of 15 drainage

experiments were performed.

## 2.4 Image Processing

An image-processing algorithm was developed to segment the raw images and characterize the spatial distributions of the two immiscible fluid phases, based on the gray-level histogram (Otsu,1979). The values of aperture occupied by the Xanthan solution were calculated by relating the binary images to the previously measured aperture field at each position (pixel by pixel). We then calculated the invading fluid saturation ($S_{nw}$), the location of the displacement front tip ($X_{tip}$), the fluid-fluid interface length ($l_{nw}$), and the local finger velocity ($v_{tip}$) for each image. The details of the image processing procedure are shown in SI Figure S3.

# 3 Results and Discussion

## 3.1 Displacement Patterns

The dynamics of the interface displacement from the start of the invasion to the breakthrough is shown for different experimental conditions of flow rate $Q$ and polymer concentration $C_p$ in Figure 3, with composite images. These images constitute an experimental phase diagram in the $Q$-$C_p$ space. Since the apparent viscosity of the invading fluid increases with $C_p$ (Figure 2b), one may also consider using dimensionless numbers (capillary number $Ca$ and viscosity ratio $M$) to replace the controlling variables $Q$ and $C_p$, as in the classical phase diagram for Newtonian fluids (Lenormand et al., 1988). However, this is not done here because the

viscosity of the invading fluid is a function of the local shear rate; hence, not only does it vary spatially within the fracture, but its value averaged over the fracture volume is a function of the prescribed flow rate. From the phase diagram (Figure 3), it can be seen that at high flow rates ($Q \geq 0.5$~5 mL/min, depending on $C_p$), the displacement shows characteristics of typical viscous fingering (VF) patterns, which resemble the behavior in the classical Lenormand phase diagram for drainage. However, a transition to capillary fingering with decreasing flow rates is not observed. Instead, a mixed displacement (MD) pattern of stable and unstable invasions emerges, where the fluid invades the rough fracture with a stable front at the beginning and then the front suddenly becomes unstable as the invasion proceeds; this behavior is different from the displacement patterns of Newtonian fluids previously observed and modelled for fractures (Chen et al., 2017; Yang et al., 2019a). In the MD regime, the onset of instability seems to occur at a larger invasion length for higher $C_p$. The mixed stable-unstable patterns are indicative of the dynamic effect brought by the non-Newtonian rheology during the displacement. When the polymer concentration is high and the flow rate is low ($C_p$ = 1wt% and $Q$ = 0.1 mL/min), the invasion front is stable, resulting in compact displacement (CD). The transitions from VF to MD to CD are marked by the solid lines in Figure 3. Previous studies have shown that for a given Newtonian fluid pair, the displacement pattern would transition from capillary fingering (CF) to compact displacement (CD) under favorable displacement condition ($M > 1$) with increasing flow rate, and the fluid-fluid interface would thus be stabilized by viscous forces (Lenormand et al., 1988; Zhang et al., 2011; Tsuji et al., 2016; Chen et al., 2018). However, in our experiments, for a given $C_p$ = 1wt%, the displacement

patterns transition from CD to MD to viscous fingering (VF), which means that the fluid-fluid interface tends to become more unstable with increasing $Q$, which would not occur if there were no shear-thinning effects.

It should be pointed out that the mixed displacement pattern for shear-thinning fluids in rough fractures has not been reported and analyzed in the literature. The mechanism for the transition between the displacement regimes will be discussed in Section 3.3 and Section 3.4.

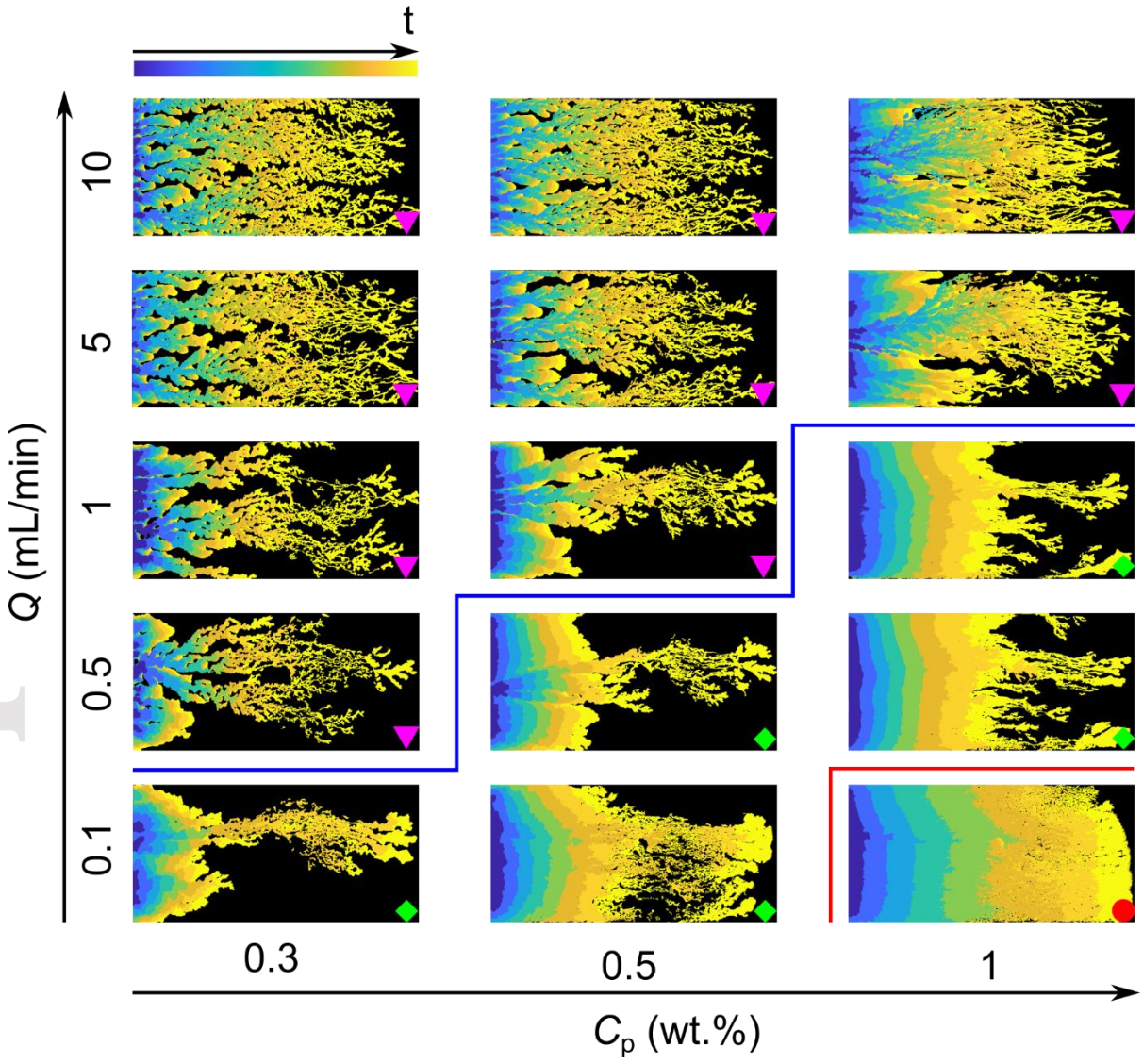


**Figure 3**. Evolution of the fluid-fluid displacement fronts until breakthrough. The polymer concentration $C_p$ increases from left to right, and the flow rate $Q$ increases from the bottom to

the top. The blue color represents the initial stage and the yellow indicates the breakthrough time. The black regions denote silicone oil. The flow direction is from left to right. The magenta down triangles mark the viscous fingering (VF) pattern, the green diamonds mark the mixed displacement (MD) pattern, and the red circle marks the compact displacement (CD) pattern.

The competition between capillary and viscous forces results in the various flow patterns. The dimensionless capillary number $Ca$ is classically used to evaluate the relative importance of viscous forces, relative to capillary forces, while the viscosity ratio $M$ controls the viscous (in)stability of the interface (Lenormand, 1990) for Newtonian fluids. Here, $Ca$ is defined as $Ca = \mu_i v_i/\sigma$, where $v_i = Q/A_c$ is the Darcy (i.e., mean) velocity of the invading fluid, $Q$ is the flow rate, $A_c$ is the cross-sectional area of the fracture's flow domain, measured at the fracture inlet, $\mu_i$ is the viscosity of the invading fluid, and $\sigma$ is the interfacial tension. The viscosity ratio $M$ is defined as: $M = \mu_i/\mu_d$, where $\mu_d$ is the viscosity of the defending fluid. In our experiments with a shear-thinning invading fluid, it is not straightforward to define a single, representative value for $\mu_i$, since the local viscosity of the invading fluid changes with the shear rate and is impacted by the aperture variability. For single-phase flow, an effective viscosity is often employed to quantify the shear-rate-dependency by using Darcy's law (Tosco et al., 2013; Rodríguez de Castro and Radilla, 2017). However, for two-phase flow, it is not reasonable to use Darcy's law to calculate the effective viscosity due to the occurrence of interface instabilities. Thus, in this work, we adopt an a priori estimate of the local viscosity averaged over the fracture to represent the effective viscosity $\mu_i$. This estimate is obtained by considering

a shear rate that is the ratio of the mean flow velocity to the local fracture aperture. In Section 3.4 (interface stability analysis), we present a detailed description of the treatment of the relationship between local viscosity and mean velocity.

The capillary number and viscosity ratio corresponding to each polymer concentration at different flow rates are presented in Figure 4a. The interplay between capillary and viscous forces is more complex when the displacing fluid is shear-thinning than with two Newtonian fluids. For example, for $C_p$ = 0.3 wt%, the value of $\log_{10}Ca$ increases only from −2.28 to −1.83 when $Q$ is increased by two orders of magnitude from 0.1 mL/min to 10 mL/min. However, for a Newtonian displacing fluid, the difference between $\log_{10}Ca$ at $Q$ = 10 mL/min and $\log_{10}$Ca at $Q$ = 0.1 mL/min should be 2, much greater than that obtained with the shear-thinning displacing fluid. Moreover, the range of $\log_{10}Ca$, corresponding to a given range of $Q$, is narrower at higher $C_p$. This is due to the decreasing dependence of $M$ on $Q$. As shown in Figure 4a, with increasing $Q$, the range of the $M$ variation is from 1.80 to 0.05 for $C_p$ = 0.3wt%, from 5.42 to 0.11 for $C_p$ = 0.5 wt%, and from 14.64 to 0.27 for $C_p$ = 1 wt%. As a result, when $Q \geq 5$ mL/min, $\log_{10}M$ becomes negative, the displacement patterns exhibit strong fingering characteristics from the start of the invasion. Note also that given the high capillary number ($\log_{10}Ca > -2.4$) in all experiments, it can be assumed that capillary forces played an insignificant role in all the experiments.

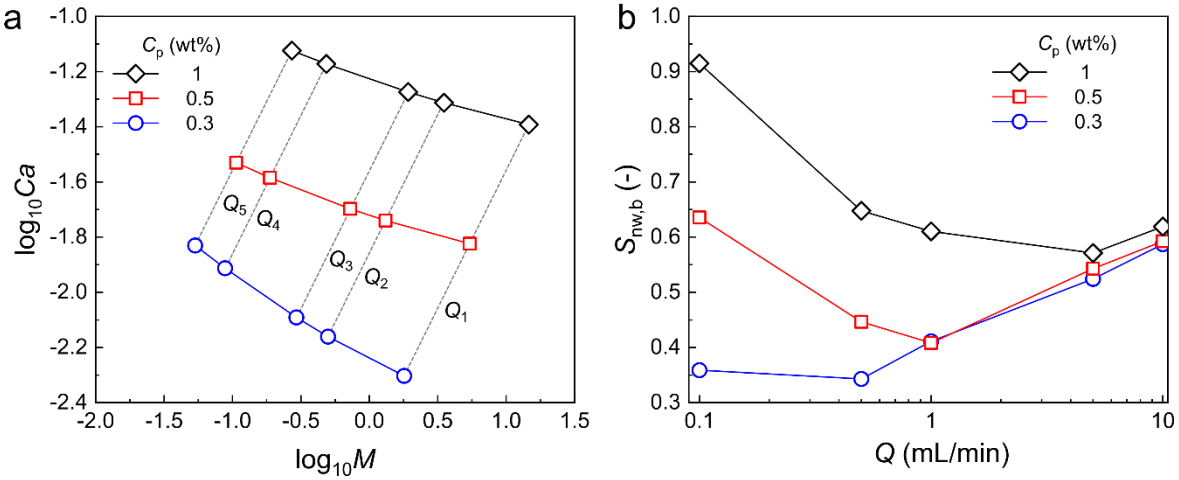


**Figure 4.** (a) Variation of $\log_{10}Ca$ (capillary number) as a function of $\log_{10}M$ (viscosity ratio) for each polymer concentration. $Q_1$−$Q_5$ represents, respectively, 0.1, 0.5, 1, 5, 10 mL/min. (b) Variation of displacement efficiency $S_{nw,b}$ with flow rate $Q$.

The displacement efficiency $S_{nw,b}$ (taken as the invading fluid saturation at the breakthrough time) is shown as a function of $Q$ in Figure 4b. $S_{nw,b}$ is calculated as the ratio of invading fluid volume to the pore volume of the fracture. The results show that the displacement efficiency is enhanced as $C_p$ increases at a given $Q$. According to Figure 4a, the values of $M$ and $Ca$ increase with $C_p$ for a constant $Q$. Generally, when $Ca$ increases, viscous forces dominate the interface displacement; they cause viscous instability when $M < 1$. On the other hand, the increase of $M$ at low flow rates causes a higher viscous pressure drop in the invading phase, which may stabilize the invasion front. At low given flow rates, the increase in $Ca$ due to an increase in $C_p$ is overwhelmed by the simultaneous increase in $M$, leading to a stable invading front (see Figure 3, bottom right part) and a high displacement efficiency ($S_{nw,b} >$ 0.9). At high flow rates ($Q \geq 5$ mL/min), the increase of $C_p$ does not result in significant changes in the displacement efficiency, because the shear-thinning effects reduce the viscosity of the

invading fluid to $M < 1$. It is also interesting to observe in Figure 4b that the displacement efficiency $S_{nw,b}$ exhibits non-monotonicity with respect to $Q$, and the non-monotonicity is especially strong for the intermediate $C_p = 0.5\%$. The non-monotonic trend of $S_{nw,b}$ is related to the shift of the invasion pattern from mixed displacement to viscous fingering regime. At low flow rates, the interface is relatively stable at the beginning of the displacement and the piston-like stable displacement invasion pattern gives a high sweep efficiency. Therefore, with increasing $Q$, the width of the stable region decreases, i.e., the onset of fingering occurs earlier, leading to decreased displacement efficiency. As $Q$ exceeds a critical value, the displacement pattern shows the characteristics of viscous fingering. Further increase in $Q$ results in a higher number of viscous fingers, and thus a larger $S_{nw,b}$.

## 3.2 Flow regime transition

Recent theoretical analysis (Martyushev and Birzina, 2015) and experimental studies (Varges et al., 2020) have shown that, for non-Newtonian fluids in a Hele-Shaw cell, the interface can be either stable and propagate uniformly, or be unstable with strong fingering behavior, depending on the effective viscosities of the invading and defending fluids. However, in our experiments with rough-walled fractures, we observe a transition between flow regimes, from stable displacement to mixed displacement and to unstable viscous fingering patterns. In order to quantitatively analyze this transition between flow regimes, we first present the evolutions of the displacement interface in a subset of our experiments (Figure 5a-e) to characterize the transition from stable to unstable front. Since the viscous forces play a

dominant role in the displacement patterns of this study, and, moreover, are dependent on the rheological properties of the xanthan gum solutions, the effect of the shear thinning rheology should be examined in detail. In particular, our experimental observations (especially for the mixed displacement patterns) suggest that the spatial and temporal variations of local viscosities, within the non-Newtonian displacing fluid, should be analyzed.

To quantify the local viscosity $\mu(\dot{\gamma})$, we define the mean shear rate of non-Newtonian fluid flow in a rough fracture as:

$$\dot{\gamma} = v_x / b_x \tag{3}$$

where $v_x = Q/b_x W$ is the average velocity at location $x$, $b_x$ is the average aperture at location $x$ and $W$ is the width of fracture. As shown in Figure 1b, the aperture $b_x$ decreases at first and then increases along the flow direction, where the shear rate shows the reverse trend according to Eq. (3). For shear-thinning fluids, the viscosity decreases as the average shear rate increases due to the nonlinear fluid rheology (see Figure 2b). As shown in Figure 5a-d, during the initial stage of displacement, the Xanthan gum solution invades the rough fracture with a relatively stable front. During this initial stage, the average aperture $b_x$ at the invading front is reduced as the invasion proceeds, and meanwhile $v_x$ increases as $b_x$ decreases (for a given $Q$), which accelerates the decrease in the local viscosity $\mu(\dot{\gamma})$ of the invading non-Newtonian fluid. Once the front has reached the position for which the aperture averaged over the transverse direction has the specific value that leads to the viscosity ratio decreasing below a critical number $M^*$, the front becomes unstable; fingers then develop and grow rapidly. On the contrary, the displacement front tends to stay stable during the entire experiment duration (e.g., the

displacement pattern shown in Figure. 5e) if the local viscosity ratio at the position of the fluid-fluid interface remains greater than the critical value $M^*$ at the minimum aperture of the fracture. To further verify this inference, additional experiments are conducted under favorable condition ($M > 1$) in the same rough fracture cell with the same flow rate range, using a Newtonian fluid (water-glycerol mixtures) as the invading fluid. As shown in Figure 6, due to the lack of shear thinning effect, there is little difference between the displacement patterns obtained for different flow rates, in contrast to the flow-rate-dependent invasion morphologies shown in Figure 3. Moreover, Figure 3 and Figure 6 show the evolutions of the fluid-fluid displacement fronts with time until breakthrough, and we can also compare the differences in the flow behavior of non-Newtonian fluids and Newtonian fluids at the same time or location. We see thatthe displacement pattern of non-Newtonian fluids changes with flow rate in a similar manner to that of Newtonian fluid with the viscosity ratio. This comparison between patterns obtained with invading Newtonian and non-Newtonian fluids confirms that the local viscosity ratio is a key factor influencing the displacement patterns in rough fractures, and that the combined influence of the shear-thinning rheology of the invading fluid and the fracture heterogeneity leads to the onset of instability and transition in flow regime during the displacement.

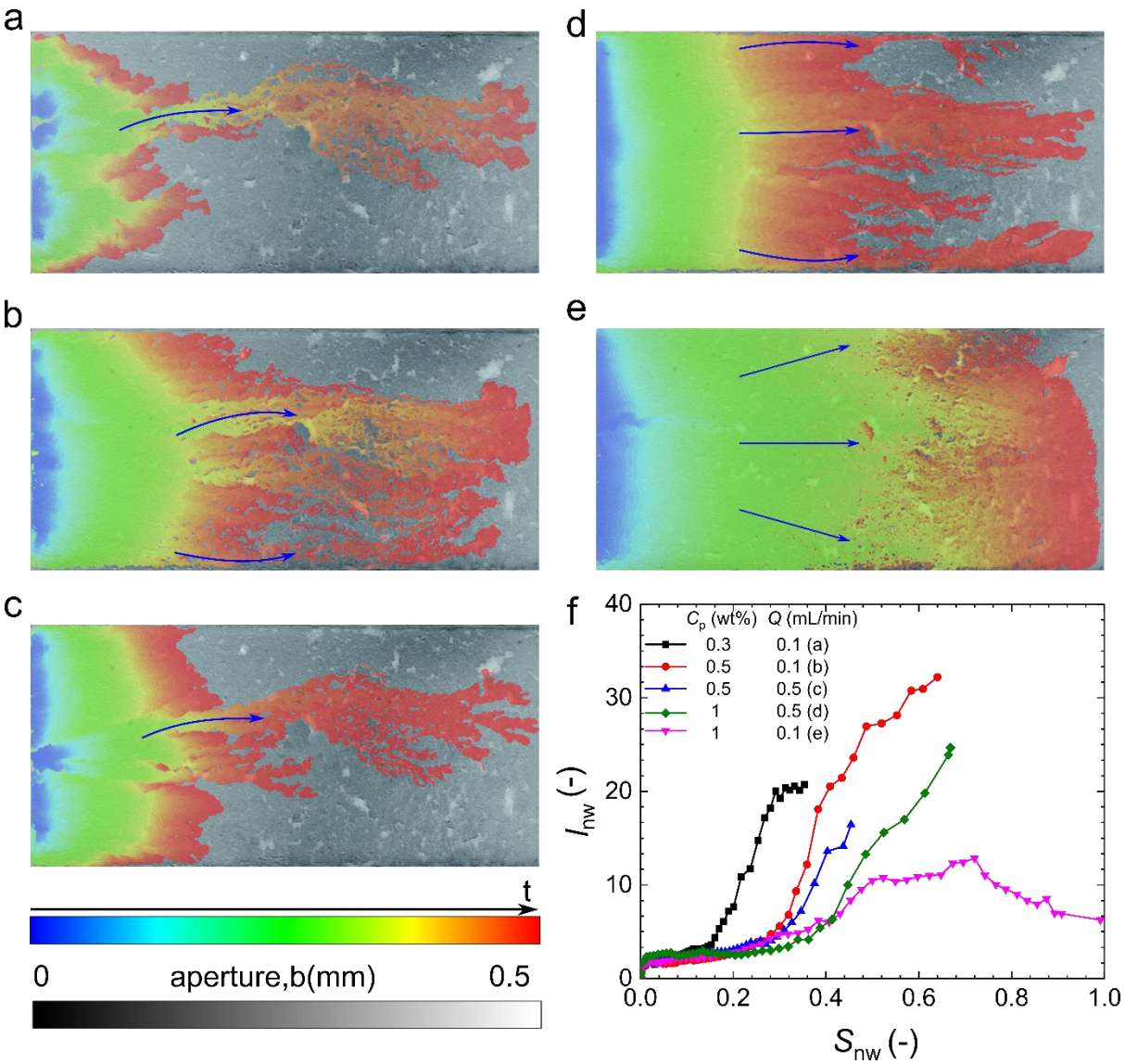


**Figure 5.** (a-e) Evolutions of the displacement front from start to breakthrough for concentrations ranging between 0.3 and 1 wt% and flow rates ranging between 0.1 and 0.5 mL/min (details are given in the legend of Fig. (f)). The blue color represents the initial stage whereas red colors indicate late times. The displacement morphologies combined with the aperture field illustrate the flow path of the invading fluid during the displacement process. The aperture field is displayed under the displacement pattern in grayscale from dark (smaller apertures) to light gray (larger apertures). (f) Evolution of the normalized fluid-fluid interface length $l_{nw}$ with the invading fluid saturation $S_{nw}$ for the displacement patterns shown in (a-e).

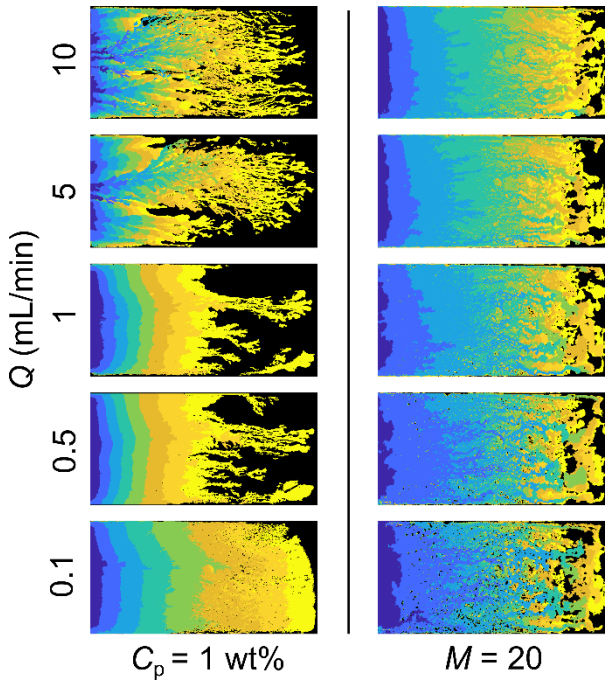


**Figure 6.** Evolutions of the fluid-fluid displacement fronts with time under shear-thinning fluid (Xanthan solutions) invading and Newtonian fluid (water-glycerol mixtures) invading conditions. The blue color represents the initial stage and the yellow indicates late times.

Furthermore, we employ the specific interface length $l_{nw}$ to characterize the dynamics of displacement (Ferrari et al., 2015; Holtzman, 2016; Chen et al., 2018). Figure 5f presents the evolutions of $l_{nw}$ with the invading fluid saturation $S_{nw}$, where $l_{nw} = L_{nw}/W$, $L_{nw}$ is the fluid-fluid interface length, including the propagating front and the regions trapped behind the front, and $W$ is the width of the fracture. The specific interface length $l_{nw}$ is an important indicator to characterize the morphology of the fluid-fluid interface. Its temporal evolution reflects the transition between invasion regimes, from a flat and stable interface (low $l_{nw}$) to a very rough and unstable interface (high $l_{nw}$). As shown in Figure 5f, for all the conditions displayed, at the beginning of displacement, the values of $l_{nw}$ are low and show small fluctuations, which means that the displacement front remains stable and exhibits a piston-type flow characteristic. With

the invasion proceeding, there is a sudden increase in $l_{nw}$ as the displacement regime transitions from stable to unstable. It should be noted that for the compact displacement regime (Figure 5e), in the middle stages of the invasion, there is a small increase in $l_{nw}$; this is due to the fact that the interface's roughness grows due to the smaller apertures, and therefore, larger relative aperture fluctuations, located at the center of fracture. But this is not an instability: the growth in $l_{nw}$ remains finite and is reverted when the apertures felt by the interface increase again.

## 3.3 Displacement front velocity

The above analysis indicates that the displacement pattern is closely related to the variation of local viscosity during the displacement, which is controlled by the local shear rate, which in turn depends not only on the local aperture, but also on the velocity of the displacement front. When the invading phase is a shear thinning fluid, a higher front velocity causes a lower local viscosity and earlier onset of fingering, for a given aperture. Figure 7a displays the normalized displacement front tip location, $x^*_{tip} = X_{tip}/L$, as a function of the dimensionless time $t^*$, where $X_{tip}$ is the distance between the front position and the inlet, and $L$ is the length of the fracture; $t^* = t/t_b$, $t_b$ is the breakthrough time. Here, a dimensionless variable $k_t$ is introduced to represent the slope of the $x^*_{tip}$-$t^*$ curve:

$$k_t = \frac{\partial x^*_{tip}}{\partial t^*} = \frac{X_{tip,i+1}/L - X_{tip,i}/L}{t_{i+1}/t_b - t_i/t_b} = \frac{v_{tip,i}}{\bar{v}} \tag{4}$$

where $i$ is the time step at which the image was captured, $L$ is the fracture length, $v_{tip,i}$ is the front velocity at time $t_i$, and $\bar{v}$ is the average front velocity during the entire drainage process. The slope of the $x^*_{tip}$-$t^*$ curve indicates the time-dependent front velocity to the average front

velocity and features a point where a sudden increase in the slope indicates the onset of interface instability. As shown in Figure 7a, at the beginning of displacement, the slope $k_t$ = 0.34±0.01, suggesting that the average front velocity is almost three times larger than that at earlier times. That is, at later times, the front advancement speeds up and localized flow channels occur. However, the slope of the $x^*_{tip}$-$t^*$ curve is insufficient to represent the main characteristics of the displacement front propagation. Here, we define a normalized velocity, $v^*_{tip}$, to quantify the displacement front velocity:

$$v^*_{tip} = \frac{v_{tip,i}}{v_i} \tag{5}$$

where $v_i$=$Q/A_c$ is the Darcy velocity of the invading fluid, $Q$ is the flow rate, $A_c$ the cross-sectional area of the inlet. Figure 7b-f present the evolutions of the dimensionless front velocity $v^*_{tip}$ with the normalized displacement front tip $x^*_{tip}$ for mixed displacement. The transition from stable to unstable can be distinguished with the crossover position $x^*_t$ at which the localized flow channel occurs and the front velocity begins to increase; such positions are marked with star symbols in Figure 7b-f. Since changes in slopes of the $x^*_{tip}$ - $t^*$ curves in Figure 7a exhibit a similar trend, we take Figure 7b as an example to analyze the front velocity evolution. At the beginning of the displacement, the displacement front advances slowly toward the outlet and the difference between the front velocity and the Darcy velocity is small, indicating a relatively uniform front and stable displacement. However, when the displacement front reaches the critical location $x^*_t$ at which the aperture is below the value that keeps the viscosity ratio above $M^*$, instability occurs and the propagation of the displacement front speeds up. In particular, as the instability occurs, the local viscosity is further reduced due to the progressively smaller

aperture and higher velocity, which is favorable to instability and finger development, as shown in Figure 7b. When the displacement front escapes the region with a negative gap gradient, the viscosity recovers and becomes larger as the aperture increases due to decrease in local shear rates, and the front velocity is thus reduced accordingly. The occurrence and development of instability thus results from the mutual promotion of front velocity increase and shear-thinning mediated viscosity decrease.

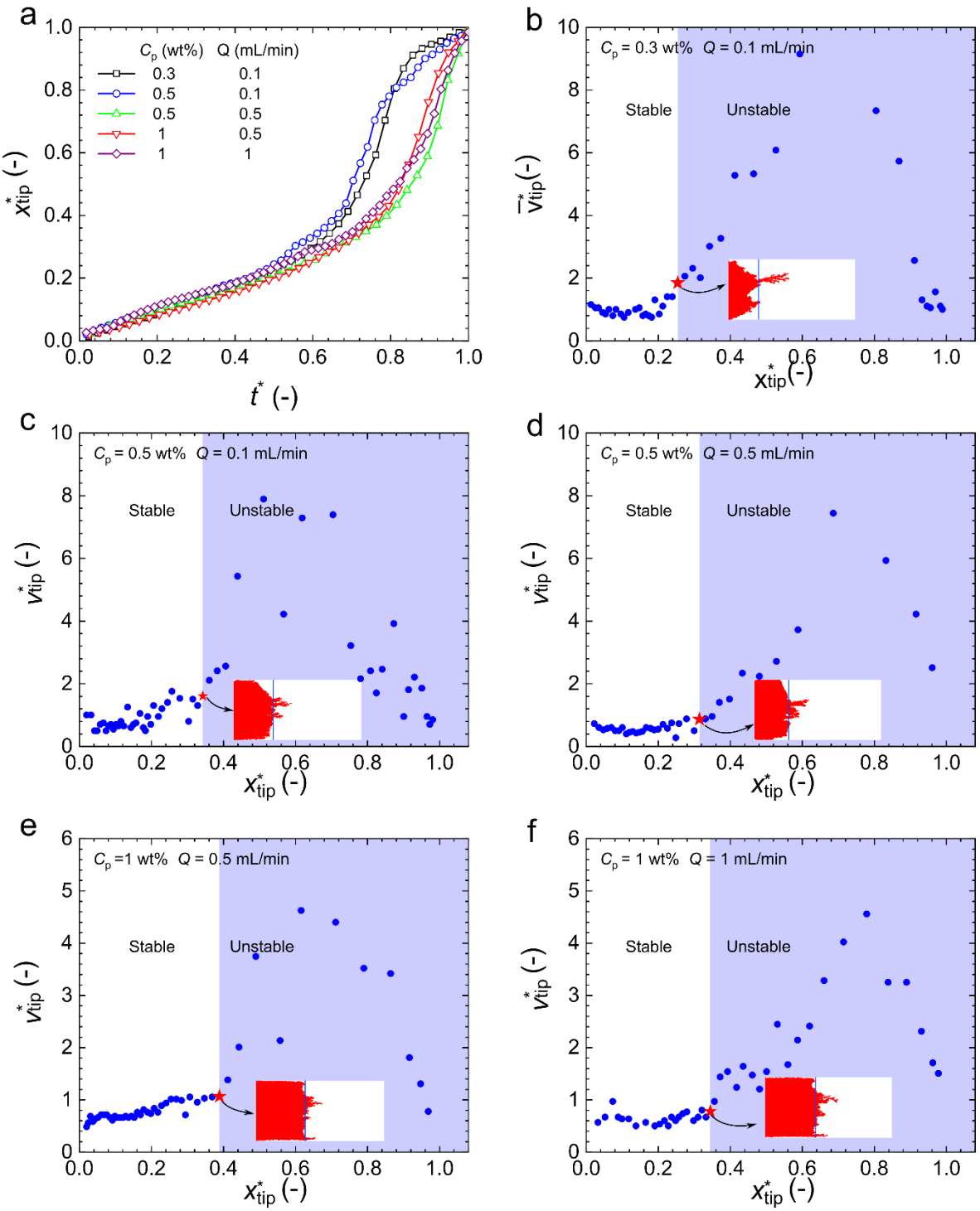


**Figure 7.** (a) Evolution of the normalized displacement front tip $x^*_{tip}$ with the dimensionless time $t^*$. (b)-(f) Evolution of the displacement front velocity $v^*_{tip}$ with the normalized displacement front tip $x^*_{tip}$. The inset in (b)-(f) shows the onset location of instability in experiments.

The location for the onset of instability is an important parameter influencing the displacement efficiency. A localized flow channel occurs when the front velocity exceeds a critical value $v_c$ that depends on the viscosity ratio $M$. According to Figure 2, the value of $M$ increases as $C_p$ increases for a constant flow rate. For a given flow rate, Eq. (2) and Eq. (3) show that the front of invading fluid with higher concentration has to advance further to reach the specific aperture region that allows it to achieve a value of local viscosity below the critical number $M^*$. As shown in Figure 8, at a given flow rate $Q = 0.1$ mL/min, the location $x_t^*$ for the onset of localized flow channel increases with polymer concentration, which is consistent with the hypothesis mentioned above. Besides, for a given polymer concentration, due to the shear-thinning behavior of the Xanthan solution, the solution displays a lower viscosity at higher shear rates, which suggests that a larger aperture (i.e., a smaller shear rate) is required to maintain a stable displacement front. Thus, the location for occurrence of instability becomes closer to the inlet as the flow rate increases (see SI Figure S4). Once the viscosity at the inlet is below $M^*$, the initial stable region vanishes and the displacement is characterized by viscous fingering from the start. The dependence of the interface velocity $v_{tip}$ on the front tip position $X_{tip}$ during the displacement provides an insight into the onset of instability controlled by the fluid rheology and heterogeneity of the rough fracture.

## 3.4 Interface stability analysis

Determining whether the interface is stable during the displacement is important for predicting the sweep/displacement efficiency in applications such as polymer flooding and rock

grouting. The mixed displacement patterns observed in our experiments provide a unique opportunity to study the onset of fingering for non-Newtonian fluid displacement. To gain a fundamental understanding of the interfacial processes, we present a theoretical model to predict the onset of instability. In our experiments, the instabilities mostly occur within the A1 region (Figure 1b) which displays a negative aperture gradient, and thus a converging Hele-Shaw cell is employed as the simplified model. A schematic of the converging configuration with a constant gap gradient is shown in Figure 8. The width and the length of the cell are taken as those for the rough fracture ($W$ = 66mm and $L$=56 mm), and its gap thickness varies linearly in the flow direction ($h(x) = h_0+\alpha x$). The gap gradient as measured in the fracture is $\alpha = -1.43\times10^{-3}$, and $h_0$ denotes the gap thickness at the inlet (located at $x = 0$). The invading fluid (Xanthan solution) with a variable viscosity $\mu_i$ displaces the defending fluid with a constant viscosity $\mu_d$, and the fluids are immiscible.

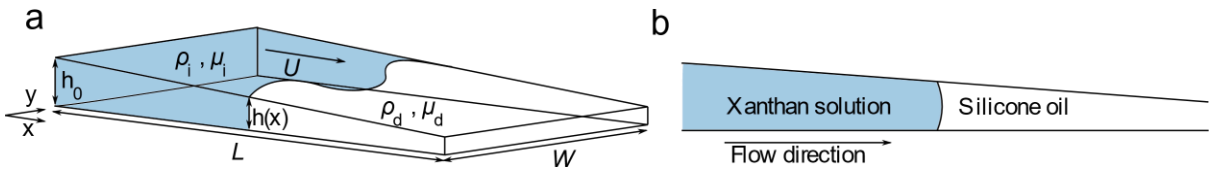


**Figure 8.** (a) Schematics of the simplified model (a converging Hele–Shaw cell with a constant depth/gap gradient). (b) Side view of the model configuration.

For Newtonian fluids, Al-Housseiny et al. (2012) have analyzed the impacts of gap gradients on the onset of interfacial instability by carrying out a linear stability analysis. In our experiments, the invading fluid is non-Newtonian and its viscosity varies with the shear rate. A common approach to deal with the non-Newtonian problems in a Hele-Shaw cell is to replace the constant viscosity $\mu$ by a shear-dependent viscosity $\mu(\dot{\gamma})$ with local shear rate $\dot{\gamma} = v / h$

(Bonn et al.,1995; Lindner et al., 2000). To obtain the local viscosity, we calculate the shear rate profile for stable flow of a yield-stress fluid between two parallel plates (a Hele-Shaw cell with aperture of $b$) within the framework of the lubrication approximation. This means that the velocity component along direction $x$ (parallel to the cell plane) is much larger than the velocity component along direction $z$ (perpendicular to the cell plane). Thus, the shear rate of Herschel–Bulkley fluid (Equation 1) can be described as:

$$\dot{\gamma} = \begin{cases} \dfrac{du}{dz} = 0, \quad |z| \le z_0 \\ \dfrac{du}{dz} = \left(\dfrac{\nabla P}{k}(z - z_0)\right)^{\frac{1}{n}}, \quad z_0 < |z| < b/2 \end{cases} \quad , z_0 = \tau_c \cdot (\nabla P)^{-1} \tag{6}$$

Integrating the above equation and assuming no slip at the wall, we obtain the vertical velocity ($u(z)$) profile:

$$u = \left(\frac{\nabla P}{k}\right)^{\frac{1}{n}} \cdot \left[ (z - z_0)^{\frac{1}{n}+1} - (\frac{b}{2} - z_0)^{\frac{1}{n}+1} \right] \frac{n}{n+1} \qquad \text{for } z_0 < |z| < b/2 \tag{7a}$$

$$u = -\left(\frac{\nabla P}{k}\right)^{\frac{1}{n}} \cdot \frac{n}{n+1} \cdot (\frac{b}{2} - z_0)^{\frac{1}{n}+1} \qquad \text{for } |z| \le z_0 \tag{7b}$$

From Equation 7 we can obtain the relationship between the mean velocity through a cross-section and local pressure gradient:

$$U = \left(\frac{\nabla P}{k}\right)^{\frac{1}{n}} \cdot \frac{n}{n+1} \cdot \left(\frac{b}{2} - z_0\right)^{\frac{1}{n}+1} \left[ \frac{n}{2n+1}(1 - \frac{bz_0}{2}) - 1 \right] \tag{8}$$

It turns out that Equation 8 can be solved for a given value of $U$ (e.g., the average velocity of a cross-section) to obtain the corresponding pressure gradient $\nabla P_c$. Then, the obtained $\nabla P_c$ can be used in Equation 6 to get the shear rate profile. Once the shear rate profile is determined,

we take the mean value of the non-zero terms of shear rate as the characteristic shear rate to calculate the invading fluid viscosity by using Equation 2. Since the experiments were conducted in a horizontal fracture cell, the influence of gravity is negligible. Based on the work of Al-Housseiny et al. (2012), the dispersion relation $\tilde{\omega}(k)$ ($\tilde{\omega}=\sigma h/U_i$ is the dimensionless growth rate and $k$ is the dimensionless wavenumber) in a tapered Hele-Shaw cell (in the limit of small $\alpha$) can be obtained as:

$$\frac{W}{h}(1+M)\tilde{\omega}=\left(1-M+\frac{2\alpha\cos\theta_c}{Ca_d}\right)k-\frac{h^2}{W^2Ca_d}k^3 \tag{6}$$

where $M=\mu_i/\mu_d$ is the viscosity ratio, $Ca_d=12\mu_d U_i/\gamma$ is the capillary number (defined for the defending phase), $U_i$ is the average velocity at the interface, and $\theta_c$ is the contact angle.

In order to obtain the wavenumber at the maximum growth rate, we take the derivative of Eq. (6) with respect to $k$. The maximum growth occurs when $\partial\tilde{\omega}/\partial k=0$ and the wavenumber $k_m$ of the maximum growth is:

$$k_m=\sqrt{\frac{2\alpha\cos\theta_c+Ca_d(1-M)}{3(h/W)^2}} \tag{7}$$

The interface will be stable when the wavenumber $k_m\le 1$, and thus the criterion for stable interface is:

$$N_c=-3(h/W)^2+2\alpha\cos\theta_c+Ca_d(1-M)\le 0 \tag{8}$$

Consequently, a theoretical criterion is established for predicting the interfacial behavior of shear-dependent fluid in a tapered cell. The criterion can be evaluated given the fluid rheological properties ($\tau_c$, $k$, $n$), average velocity $U_i$ and gap thickness $h$ at the interface, gap gradient $\alpha$, contact angle $\theta_c$ and interfacial tension $\gamma$. Here, we select several important

parameters to evaluate the impact of the fluid's (rheological) and fracture's geometric (i.e., aperture and its gradient) properties on the dimensionless number $N_c$. The variations of $N_c$ with the injection flow rate $Q$ under different parameter sets are shown in Figure 9. A summary of the parameters used for each set is listed in SI Table S1. For all the parameter combinations, $N_c$ exhibits non-monotonicity with respect to $Ca_d$. At a given value of $Ca_d$, the impact of the aperture gradient $\alpha$ on $N_c$ is relatively small (Figure 9a), as the changes only influence the term $2\alpha\cos\theta$, which is a constant value for each given $\alpha$. Figure 9b shows that $N_c$ is strongly influenced by the aperture/gap thickness; the critical capillary number for stability transition (i.e., $N_c = 0$) increases from 0.1 to 0.5 (which is equivalent to an increase in flow rate by approximately 125 times), when the aperture changes from 0.1 mm to 0.5 mm. This is due to the impact of changes in gap thickness $h$ on the term $-3(h/W)^2$ and the viscosity ratio $M$. Figure 9c shows that increasing $\tau_c$ leads to smaller (more negative) $N_c$ and thus more stable displacement; this is expected as larger values of $\tau_c$ mean higher apparent viscosities of the non-Newtonian fluid. Moreover, the rheological parameter $n$ also has an important impact on $N_c$, as shown in Figure 9d. With the increase of $n$, the shear-thinning behavior of the non-Newtonian fluid is reduced and thus the invading fluid maintains a higher viscosity; in particular, at $n > 0.5$, $N_c$ is smaller than 0 even at a very large capillary number, indicating a stable displacement for a wide range of flow rates. Figure 9e indicates that when decreasing the defending fluid viscosity $\mu_d$, one should expect a significant shift in the $N_c$- $Ca_d$ curve, especially at large capillary numbers. This is because changing the defending fluid viscosity $\mu_d$ simultaneously affects the capillary number $Ca_d$ and the viscosity ratio $M$.

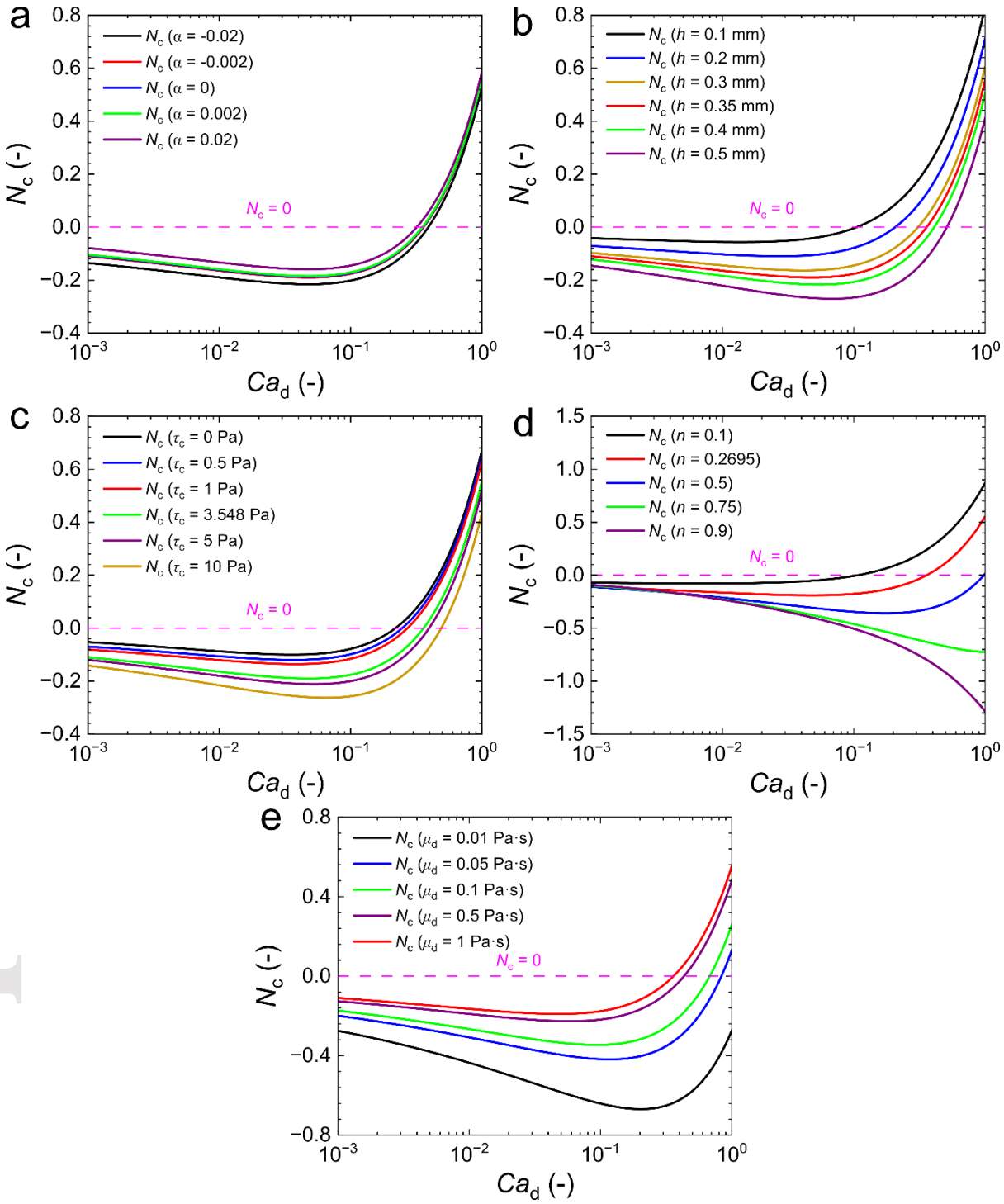


**Figure 9**. Variation of the dimensionless number $N_c$ with capillary number $Ca_d$ for different parameters. (a) aperture gradient $\alpha$. (b) aperture $h$. (c) yield stress parameter $\tau_c$. (d) rheological index $n$. (e) defending phase viscosity $\mu_d$. The critical value of $N_c = 0$ is indicated by dashed

lines. The red lines in Figure 9 represent the case for $C_p = 0.5$ wt% in our experiments.

Furthermore, we confront the theoretical predictions based on Eq. (8) to the experimental results. Using the experimental values of $U_i$, $h$ and $\alpha$, we plot the stability diagram for the interface at the inlet of the fracture, i.e., A1 (Figure 10a). It can be seen that the theoretical criterion $N_c = 0$ separates the stable and unstable patterns of interface advancement well, which confirms the validity of the proposed theory. When the invading fluid advances from A1 to the region of A2, the related model parameters (i.e., aperture and its gradient) are different and the corresponding values of $N_c$ and stability criterion predicted by the theoretical model are presented in Figure 10b. It can be seen from Figure 10b that again, the theoretical predictions of interface stability at A2 is in good agreement with the experimental results. Compared with A1, the values of $N_c$ for A2 for all the experiments increase slightly due to the decrease of $h$ and the increase of $\alpha$. In other words, during the displacement process, the interface tends to be more unstable in A2 than in A1, which is consistent with our experimental observations (i.e., mixed displacement patterns with stable interface in A1 and unstable interface in A2). Moreover, a converging Hele-Shaw cell has been demonstrated to be able to suppress the development of fingering under unfavorable conditions for Newtonian fluids (Al-Housseiny et al., 2012), and our experiments of Newtonian fluids have also confirmed this mechanism (green diamonds in Figure 10). The opposite behavior found in the results for the shear-thinning fluids demonstrates the dependence of displacement patterns on rheological properties. The above discussion indicates that the theoretical analysis based on this simplified model can capture the

transition of interface from stable to unstable on the whole and give an effective way to predict the interfacial behavior of two-phase flow in rough fracture including shear-thinning effects.

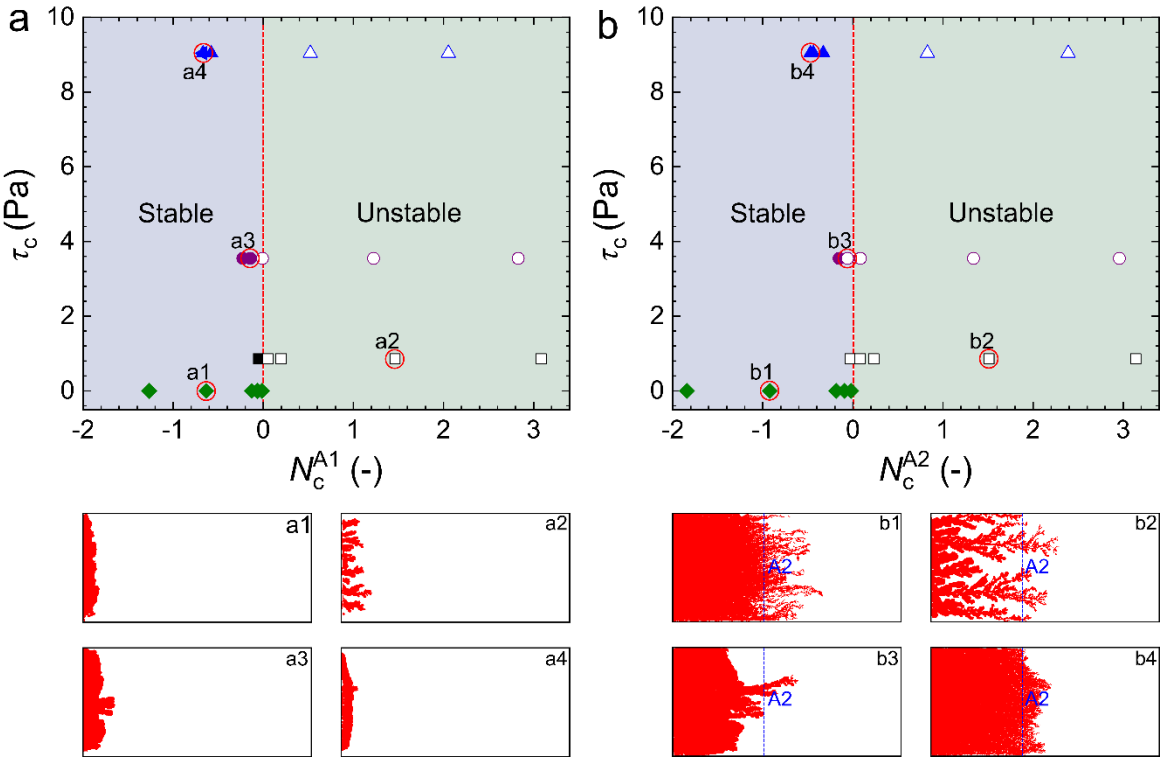


**Figure 10**. A stability diagram mapped in the $\tau_c$-$N_c$ plane for experimental results in a rough fracture. (a) $N_c$ evaluated at the inlet of A1: $U_i$ = 0.072 ~ 7.2 mm/s, $h$ = 0.35 mm and $\alpha$ = –1.43×10$^{-3}$. (b) $N_c$ evaluated at the inlet of A2: $U_i$ = 0.094 ~ 9.4 mm/s, $h$ = 0.27 mm and $\alpha$ = –9.48×10$^{-4}$. Experiments for $C_p$ = 0.3 wt%, $C_p$=0.5 wt%, $C_p$=1 wt% are denoted by squares, circles, and triangles, respectively; experiments with water-glycerol mixtures are denoted by diamonds. The theoretical boundary between stable (filled symbols) and unstable interface (open symbols) is indicated by red dashed lines $N_c$ = 0. The invasion images (labeled with open circle) for the corresponding displacement processes are shown at different times in a1-a4 and b1-b4.

## 4 Discussion

This paper has presented an experimental and theoretical study of the combined effects of shear-thinning rheology and aperture variability on two-phase flow patterns in a rough fracture, which has, to our knowledge, not been reported before. The existence of aperture variability and mean aperture gradient makes it easier to analyze the factors that influence the flow regime transition in a single fracture. Based on the experimental results and theoretical analysis, we have shown that spatial variations of aperture have a great impact on the interfacial morphology of multiphase flow involving shear-thinning fluids. An aperture field with an average longitudinal trend that is decreasing tends to destabilize the fluid-fluid interface during the displacement. Although the results are obtained from experimental observations in a specific fracture with a mean longitudinal aperture profile that first decreases continuously, before increasing continuously again, the theoretical analysis and models are general and applicable to other conditions. Given that the theoretical model considers the influence of mean aperture and large scale aperture variations on interface stability, as a result, the fluid flow behavior in fractures with different geometry can be considered by tuning these two parameters. In particular, the displacement behavior is mostly controlled by the mean aperture profiles of the fracture, which is a common parameter used for describing fractures. Moreover, the conclusions obtained from the theoretical model are not restricted to a specific fracture realization. Depending on the mean aperture and imposed flow rate, transition in the displacement regime will occur somewhere in the fracture plane, or not, depending on the value of the characteristic non-dimensional number $N_c$. In summary, for non-Newtonian two-phase

flow, when another fracture sample is involved, the spatial distribution of the displacement patterns might be different from our experimental observations, but the criteria for determining whether transition occurs in the displacement regime remain valid. In addition, this behavior will play a significant role if such longitudinal aperture gradients exist over length scales that are significant with respect to the fracture size. Here, no correlation length is seen in the aperture data, or, in other words, the correlation length is equal to the fracture length. More generally, such effects will be significant if the correlation length is not much smaller than the fracture size.

It has been shown that the Hurst exponent of fracture surface influences the displacement pattern (Auradou et al., 2001; Ye et al., 2015; Wang et al., 2023). Generally, a higher *H* means a smoother aperture variation at smaller scales compared to larger scale aperture variations, while low values of *H* often indicate the contrary (Seybold et al., 2020). During quasi-static displacement in fractures, the capillary fingering patterns for Newtonian fluids can be influenced by the roughness and Hurst exponent (Ye et al., 2015). However, when the displacement pattern transitions from capillary to viscous fingering, the displacement behavior is more strongly controlled by viscous forces, and the roughness (or more specifically the Hurst exponent) may not play a dominant role in controlling the interface stability. For non-Newtonian fluids with a dynamic range of viscosities, the impact of the Hurst exponent is expected to be reduced further. In our experiments, the fracture's recorded aperture field has a Hurst exponent slightly above 0.5. This value is somewhat low for granite fractures (whose Hurst exponent is usually close to 0.8). This difference could be due to the hardening process

of epoxy after molding from the real rock fracture (which could influence the apertures at high spatial frequencies) or due to measurements errors (equivalent to local averaging) when measuring the aperture field from light transmission measurements (Detwiler et al., 1999). In the first case the Hurst exponent of the epoxy replicas would really be 0.5 but it would be lower than the real fracture walls' Hurst exponent; in the second case the 0.5 measurement would be an underestimation of the true Hurst exponent. In any case, although the value of the Hurst exponent might slightly influence the position of the flow regime transition, we do not expect it to strongly affect the phenomenology of the transition in displacement patterns, which is mostly controlled by the fluid rheological properties, the flow rate conditions, and the large-scale aperture fluctuations (remember that single phase Newtonian flow is rough fractures is mostly controlled by aperture fluctuations at the larger scales, see e.g., Méheust (2002)).

This work is of practical significance for subsurface engineering applications including rock grouting, groundwater remediation and enhanced oil recovery. For example, in rock grouting, the effectiveness of sealing depends on the stability of the displacement front; strong fingering and early breakthrough of grouting material is usually undesirable. The results of our study suggest that the grouting front tends to destabilize in small aperture areas rather than large aperture areas. On the other hand, the grouting front stability may be improved by reducing the flow rate or increasing the polymer concentration. In future work, other important factors, include the effects of various fluid rheology, gravity, wettability, and fracture roughness, need to be further investigated.

# 5 Conclusion

We have studied the impact of the displacing fluid's rheology on two-phase flow (drainage) patterns in rough fractures by performing a series of flow visualization experiments in which Xanthan gum solutions displace silicone oil. Based on the experimentally-recorded time evolution of the displacement fronts, we have characterized the effects of the polymer concentration on the interfacial patterns and displacement efficiency. We have thus observed and characterized a hitherto-unknown mixed displacement pattern, in which the fluid-fluid interface displacement regime transitions from stable (plug flow) to unstable (fingering) as the interface advances and encounters aperture variations during the displacement process. Based on the quantitative analyses of the invasion morphologies, we have showed that this interface transition can be attributed to the coupled effect of the shear-thinning rheology of the displacing fluid and the aperture variability in the fracture, whose coupling causes the local viscosity of the displacing fluid to become smaller than that of the Newtonian displaced fluid. We have thus demonstrated the potentially-important role of fluid rheology in immiscible two-phase flow processes in rough fractures. Finally, we have proposed a theoretical criterion to explain the interface stability and predicts where in the fracture it occurs, considering the influence of fluid properties and aperture variations. The theoretical predictions are consistent with the experimental observations.

This work not only improves our understanding of the dynamics of displacement process including shear-thinning effects in rough fractures, but also has practical implications for engineering applications such as fractured rock grouting, enhanced oil recovery, and

groundwater remediation, where control of the displacement front and prediction of displacement efficiency are key assets. Our findings will provide helpful guidance on the selection of the injection rate when employing shear-thinning fluids in the aforementioned applications.

**ACKNOWLEDGEMENTS**

Funding support by the National Natural Science Foundation of China (Grant Nos. 51988101, 42077177 and 51925906) is acknowledged.

## Open Research

The generated experimental data for producing the results in this study can be obtained at (Yang, 2023).

### References

Airiau, C., & Bottaro, A. (2020), Flow of shear-thinning fluids through porous media, *Advances in Water Resources*, *143*, 103658.

Al-Housseiny, T. T., Tsai, P. A., & Stone, H. A. (2012), Control of interfacial instabilities using flow geometry, *Nature Physics*, *8*(10), 747-750.

Amundsen, H. K., Wagner, G., Oxaal, U., Meakin, P., Feder, J., & Jøssang, T. J. (1999), Slow two-phase flow in artificial fractures: Experiments and simulations, *Water Resources Research*, *35*(9), 2619–2626.

An, S., Sahimi, M., & Niasar V. (2022), Upscaling Hydrodynamic Dispersion in non-Newtonian Fluid Flow through Porous Media, *Water Resources Research*, 58(10), e2022WR032238.

Auradou, H., Boschan, A., Chertcoff, R., Gabbanelli, S., Hulin, J. P., & Ippolito, I. (2008), Enhancement of velocity contrasts by shear-thinning solutions flowing in a rough fracture, *Journal of Non-Newtonian Fluid Mechanics*, *153*(1), 53-61.

Auradou, H., Hulin, J.-P., & Roux, S. (2001), Experimental study of miscible displacement fronts in rough self-affine fractures, *Physical Review E*, 63(6), 066306.

Barbati, A. C., Desroches, J., Robisson, A., & McKinley, G. H. (2016), Complex Fluids and Hydraulic Fracturing, Annual Review of Chemical and Biomolecular Engineering, 7(1), 415-453.

Berkowitz, B. (2002), Characterizing flow and transport in fractured geological media: A review, *Advances in Water Resources*, *25*(8-12), 861-884.

Bonn, D., Kellay, H., Amar, M. B., & J. Meunier (1995), Viscous finger widening with surfactants and polymers, *Physical Review Letters*, *75*(11), 2132.

Boschan, A., Auradou, H., I. Ippolito, Chertcoff, R., & Hulin, J.-P. (2007), Miscible displacement fronts of shear thinning fluids inside rough fractures, *Water Resources Research*, *43*(3), 2006WR005324

Buka, A., Kertész, J., & Vicsek, T. (1986), Transitions of viscous fingering patterns in nematic liquid crystals, Nature, 323(6087), 424-425.

Chen, Y. F., S. Fang, D. S. Wu, & R. Hu (2017), Visualizing and quantifying the crossover from capillary fingering to viscous fingering in a rough fracture, *Water Resources Research*, *53*(9), 7756-7772.

Chen, Y.-F., Wu, D.-S., Fang, S., & Hu, R. (2018), Experimental study on two-phase flow in rough fracture: Phase diagram and localized flow channel, *International Journal of Heat and Mass Transfer*, *122*, 1298-1307.

Coussot, P. (2014), Yield stress fluid flows: A review of experimental data, *Journal of Non-Newtonian Fluid Mechanics*, *211*, 31-49.

Coussot, P. (1999), Saffman–Taylor instability in yield-stress fluids, *Journal of Fluid Mechanics*, *380*, 363-376.

da Silva, J. A., Kang, P. K., Yang, Z., Cueto-Felgueroso, L., & Juanes, R. (2019), Impact of confining stress on capillary pressure behavior during drainage through rough fractures, *Geophysical Research Letters*, *46*(13), 7424-7436.

de Dreuzy, J.-R., Méheust, Y., & Pichot, G. (2012), Influence of fracture scale heterogeneity on the flow properties of three-dimensional discrete fracture networks (DFN), *Journal of Geophysical Research: Solid Earth*, 117(B11).

De, S., P. Krishnan, J. Schaaf, J. Kuipers, & J. T. Padding (2017), Viscoelastic effects on residual oil distribution in flows through pillared microchannels, *Journal of Colloid & Interface Science*, *510*.

Detwiler, R. L., H. Rajaram, & R. J. Glass (2009), Interphase mass transfer in variable aperture fractures: Controlling parameters and proposed constitutive relationships, *Water resources research*, *45*(8).

Detwiler, R. L., Pringle, S. E., & Glass, R. J. (1999). Measurement of fracture aperture fields using transmitted light: An evaluation of measurement errors and their influence on simulations of flow and transport through a single fracture. *Water Resources Research*, 35(9), 2605-2617.

Fast, P., L. Kondic, M. J. Shelley, & P. Palffy-Muhoray (2001), Pattern formation in non-Newtonian Hele–Shaw flow, *Physics of Fluids*, *13*(5), 1191-1212.

Ferrari, A., Jimenez-Martinez, J., Borgne, T. L., Méheust, Y., & Lunati, I. (2015). Challenges in modeling unstable two-phase flow experiments in porous micromodels. *Water Resources Research*, 51(3), 1381-1400.

Géraud, B., S. A. Jones, I. Cantat, B. Dollet, & Y. Méheust (2016), The flow of a foam in a two ‐ dimensional porous medium, *Water Resources Research*, 52(2), 773-790.

Glass, R. J., Nicholl, M. J., & Yarrington, L. (1998), A modified invasion percolation model for low-capillary number immiscible displacements in horizontal rough-walled fractures: Influence of local in-plane curvature, *Water Resources Research*, *34*(12), 3215-3234.

Hauswirth, S. C., Abou Najm, M. R., & Miller, C. T. (2019), Characterization of the pore structure of porous media using non ‐ Newtonian fluids, *Water Resources Research*, 55(8), 7182-7195.

Herschel, W. H., & Bulkley, R. (1926), Konsistenzmessungen von Gummi-Benzollösungen, *Kolloid-Zeitschrift*, *39*(4), 291-300.

Holtzman, R. (2016), Effects of pore-scale disorder on fluid displacement in partially-wettable porous media, *Scientific reports*, *6*(1), 1-10.

Hu, R., Wu, D.S., Yang, Z. & Chen, Y.F., (2018). Energy conversion reveals regime transition of imbibition in a

rough fracture. *Geophysical Research Letters*, 45(17), pp.8993-9002.

Hu, R., Zhou, C. X., Wu, D. S., Yang, Z., & Chen, Y. F. (2019), Roughness control on multiphase flow in rock fractures, *Geophysical Research Letters*, *46*(21), 12002-12011.

Isakov, E., Ogilvie, S. R., Taylor, C. W., & Glover, P. W. (2001), Fluid flow through rough fractures in rocks I: high resolution aperture determinations, *Earth and Planetary Science Letters*, *191*(3-4), 267-282.

Kawaguchi, M., Makino, K. & Kato, T. (1997), Viscous fingering patterns in polymer solutions, *Physica D: Nonlinear Phenomena*, *109*(3-4), 325-332.

Kondic, L., Shelley, M. J., & Palffy-Muhoray, P. (1998), Non-newtonian hele-shaw flow and the saffman-taylor instability, *Physical Review Letters*, *80*(7), 1433.

Lavrov, A. (2013), Redirection and channelization of power-law fluid flow in a rough-walled fracture, *Chemical Engineering Science*, *99*, 81-88.

Lemaire, E., Levitz, P., Daccord, G., & Van Damme, H. (1991), From viscous fingering to viscoelastic fracturing in colloidal fluids, Phys Rev Lett, 67(15), 2009-2012.

Lenci, A., Putti, M., Di Federico, V., & Méheust, Y. (2022a). A Lubrication-Based Solver for Shear-Thinning Flow in Rough Fractures. Water Resources Research, 58(8), e2021WR031760.

Lenci, A., Méheust, Y., Putti, M., & Di Federico, V. (2022b). Monte Carlo Simulations of Shear-thinning Flow in Geological Fractures. Water Resources Research, 58(9), e2022WR032024.

Lenormand, R., Touboul, E., & Zarcone, C. (1988), Numerical models and experiments on immiscible displacements in porous media, *Journal of fluid mechanics*, *189*, 165-187.

Lenormand, R. (1990), Liquids in porous media, Journal of Physics: Condensed Matter, 2(S), SA79.

Lindner, A., Coussot, P., & Bonn, D. (2000), Viscous Fingering in a Yield Stress Fluid, *Physical Review Letters*, *85*(2), 314-317.

Martyushev, L., & Birzina, A. (2015), Morphological stability of an interface between two non-Newtonian fluids moving in a Hele-Shaw cell, *Physical Review E*, *91*(1), 013004.

Méheust, Y., Flow in open fractures, PhD thesis, University Paris-Sud, 2002.

Nittmann, J., Daccord, G., & Stanley, H. E. (1985), Fractal growth viscous fingers: quantitative characterization of a fluid instability phenomenon, *Nature*, *314*(6007), 141-144.

Odling, N. E. (1994), Natural fracture profiles, fractal dimension and joint roughness coefficients, *Rock Mechanics and Rock Engineering*, 27, 135-153.

Osiptsov, A. A. (2017), Fluid Mechanics of Hydraulic Fracturing: a Review, *Journal of Petroleum Science and Engineering*, *156*, 513-535.

Otsu, N. (1979), A threshold selection method from gray-level histograms, *IEEE transactions on systems, man, and cybernetics*, *9*(1), 62-66.

Persoff, P., & Pruess, K. (1995), Two-phase flow visualization and relative permeability measurement in natural rough-walled rock fractures, *Water resources research*, *31*(5), 1175-1186.

Poole, R. J. (2016), Elastic instabilities in parallel shear flows of a viscoelastic shear-thinning liquid, *Phys.rev.fluids*, *1*(4).

Raimbay, A., Babadagli, T., Kuru, E., & K. Develi (2016), Quantitative and visual analysis of proppant transport in rough fractures, *Journal of Natural Gas Science & Engineering*, 1291-1307.

Rodríguez de Castro, A., & Radilla, G. (2017), Flow of yield stress and Carreau fluids through rough-walled rock fractures: Prediction and experiments, *Water Resources Research*, *53*(7), 6197-6217.

Rodríguez de Castro, A., & Goyeau, B. (2022), Numerical analysis of the pore-scale mechanisms controlling the

efficiency of immiscible displacement of a pollutant phase by a shear-thinning fluid, *Chemical Engineering Science*, *251*, 117462.

Schmittbuhl, J., Steyer, A., Jouniaux, L., & Toussaint, R. (2008), Fracture morphology and viscous transport, *International Journal of Rock Mechanics and Mining Sciences*, 45(3), 422-430.

Seybold, H., Carmona, H. A., Leandro Filho, F., Araújo, A., Nepomuceno Filho, F., & Andrade Jr, J. (2020), Flow through three-dimensional self-affine fractures, *Physical Review Fluids*, 5(10), 104101.

Shah, C., & Yortsos, Y. (1995), Aspects of flow of power-law fluids in porous media, *AIChE Journal*, *41*(5), 1099-1112.

Silva, J., Smith, M. M., Munakata-Marr, J., & J. E. Mccray (2012), The effect of system variables on in situ sweep-efficiency improvements via viscosity modification, *Journal of Contaminant Hydrology*, *136-137*, 117-130.

Song, K.-W., Kim, Y.-S., & Chang, G.-S. (2006), Rheology of concentrated xanthan gum solutions: Steady shear flow behavior, *Fibers and Polymers*, *7*(2), 129-138.

Sorbie, K. S. (2013), *Polymer-improved oil recovery*, Springer Science & Business Media.

Tosco, T., & Sethi, R. (2010), Transport of Non-Newtonian Suspensions of Highly Concentrated Micro- And Nanoscale Iron Particles in Porous Media: A Modeling Approach, *Environmental Science & Technology*, *44*(23), 9062.

Tosco, T., Marchisio, D. L., Lince, F., & Sethi, R. (2013), Extension of the Darcy-Forchheimer law for shear-thinning fluids and validation via pore-scale flow simulations, *Transport in Porous Media*, *96*(1), 1-20.

Tsuji, T., Jiang, F., & Christensen, K. T. (2016), Characterization of immiscible fluid displacement processes with various capillary numbers and viscosity ratios in 3D natural sandstone, *Advances in Water Resources*, *95*, 3-15.

Varges, P., Azevedo, P., Fonseca, B., de Souza Mendes, P., Naccache, M., & Martins, A. (2020), Immiscible liquid-liquid displacement flows in a Hele-Shaw cell including shear thinning effects, *Physics of Fluids*, *32*(1), 013105.

Wang, Y., Zhang, Z., Ranjith, P. G., & Han, X. (2023), Flow structure transition and identification of two-phase fluid flow through rough rock fractures, *The European Physical Journal Plus*, 138(5), 376.

Whitcomb, P. J., & Macosko, C. (1978), Rheology of xanthan gum, *Journal of Rheology*, *22*(5), 493-505.

Yang, Z. (2023). Experimental data for "Displacement patterns of a Newtonian fluid by a shear-thinning fluid in a rough fracture" [Dataset], HydroShare, https://doi.org/10.4211/hs.ea239c1052644e989e5440923d90a74a

Yang, Z., Niemi, A., Fagerlund, F., & Illangasekare, T. (2013). Two-phase flow in rough-walled fractures: Comparison of continuum and invasion-percolation models. Water resources research, 49(2), 993-1002.

Yang, Z., Neuweiler, I., Méheust, Y., Fagerlund, F., & Niemi, A. (2016). Fluid trapping during capillary displacement in fractures. Advances in Water Resources, 95, 264-275.

Yang, Z., Li, D., Xue, S., Hu, R., & Chen, Y.-F. (2019a), Effect of aperture field anisotropy on two-phase flow in rough fractures, *Advances in Water Resources*, *132*, 103390.

Yang, Z., Méheust, Y., Neuweiler, I., Hu, R., Niemi, A., & Y.-F. Chen (2019b), Modeling immiscible two-phase flow in rough fractures from capillary to viscous fingering, *Water Resources Research*, *55*(3), 2033-2056.

Ye, Z., Liu, H.-H., Jiang, Q., & Zhou, C. (2015), Two-phase flow properties of a horizontal fracture: The effect of aperture distribution, *Advances in Water Resources*, 76, 43-54.

Zami-Pierre, F., De Loubens, R., Quintard, M., & Davit, Y. (2016), Transition in the flow of power-law fluids through isotropic porous media, *Physical review letters*, *117*(7), 074502.

Zhang, C., Oostrom, M., Wietsma, T. W., Grate, J. W., & Warner, M. G. (2011), Influence of Viscous and Capillary

Forces on Immiscible Fluid Displacement: Pore-Scale Experimental Study in a Water-Wet Micromodel Demonstrating Viscous and Capillary Fingering, *Energy & Fuels*, 25, 3493-3505.

Zhang, M., Prodanović, M., Mirabolghasemi, M., & Zhao, J. (2019), 3D microscale flow simulation of shear-thinning fluids in a rough fracture, *Transport in Porous Media*, *128*(1), 243-269.

Zou, L., Håkansson, U., & Cvetkovic, V. (2018). Two-phase cement grout propagation in homogeneous water-saturated rock fractures. International Journal of Rock Mechanics and Mining Sciences, 106, 243-249.

Mehr, N., C. Roques, Y. Méheust, S. Rochefort, and J. S. Selker (2020), Mixing and finger morphologies in miscible non-Newtonian solution displacement, Experiments in Fluids, 61(4), 96.

de Castro and Radilla (2017)" refers to "Rodríguez de Castro, A., and G. Radilla (2017), Flow of yield stress and Carreau fluids through rough-walled rock fractures: Prediction and experiments, Water Resources Research, 53(7), 6197-6217

Yan, Y., and J. Koplik (2008), Flow of power-law fluids in self-affine fracture channels, Phys Rev E Stat Nonlin Soft Matter Phys, 77(3 Pt 2), 036315

Boronin, S. A., A. A. Osiptsov, and J. Desroches (2015), Displacement of yield-stress fluids in a fracture, International Journal of Multiphase Flow, 76, 47-63